VSC-HVDC transmission line fault location based on transient characteristics

YANXIA ZHANG, ANLU BI ⓘ, JIAN WANG, FUHE ZHANG, JINGYI LU

School of Electrical and Information Engineering, Tianjin University
China

e-mail: anlu96@tju.edu.cn

Abstract: Accurate and reliable fault location is necessary for ensuring the safe and reliable operation of the VSC-HVDC transmission system. This paper proposed a single-terminal fault location method based on the fault transient characteristics of the two-terminal VSC-HVDC transmission system. The pole-to-pole transient fault process was divided into three stages, the time-domain expression of the DC current during the diode freewheel stage was used to locate the fault point, and a criterion for judging whether the fault evolves to the diode freewheel stage was proposed. Taking into account the enhancing effect of the opposite system to the fault current, the DC side pole-to-ground fault network was equated to a fourth-order circuit model, the relationship of fault distance with the characteristic roots of fault current differential equation was derived, and the Prony algorithm was utilized for data-fitting to extract characteristic roots to realize fault location. A two-terminal VSC-HVDC transmission system was modelled in PSCAD/EMTDC. The simulation result verifies that the proposed principle can accurately locate the fault point on the VSC-HVDC transmission lines.

Key words: characteristic roots, fault location, identification of fault stages, Prony algorithm, VSC-HVDC

1. Introduction

With the development of power electronics technology, voltage source converter-based high voltage direct current (VSC-HVDC) technology has made rapid progress. VSC-HVDC adopts bidirectional controllable power electronic devices, can control both active and reactive power simultaneously, is suitable for long-distance power transmission, distributed energy interconnection, power grid interconnection, and other fields [1, 2]. However, high voltage direct current

(HVDC) transmission lines have relatively high fault possibility because of the complex geographical environment and poor working conditions, and are difficult to manual inspect due to the fast reaction of protection and the inapparent external fault performance. Therefore, the research on VSC-HVDC transmission line fault location is of great theoretical significance and practical value for improving the reliability of the power system.

The existing VSC-HVDC transmission line fault location method can be divided into three categories [3, 4]: the traveling wave method [5–9], the natural frequency method [10–12], and the fault analysis method [14–18]. The traveling wave method locates the fault point according to the relationship among the traveling wave arrival time at the direct current (DC) bus, traveling wave velocity, and the fault distance. In order to extract the traveling wave arrival time at the DC bus, the wavelet transform is applied in [8], it can effectively extract the characteristics of the fault traveling wave and eliminate the impact of dispersion, but the extraction accuracy is affected by the transform scale. In order to obtain a relatively accurate wave velocity, reference [9] utilizes the distributed traveling wave detection device to detect the traveling wave propagation time for a transmission line of known length, then the wave velocity can be calculated, but the distributed traveling wave detection device increases the cost. The natural frequency refers to a series of harmonic components that constitute the fault transient traveling wave spectrum, among them, the harmonic component with the lowest frequency and the largest amplitude is the dominant natural frequency. The natural frequency method located the fault point according to the functional relationship between the dominant natural frequency and the fault distance, it does not need to detect the traveling wave head. And the precise extraction of the dominant natural frequency is the key to locate accurately. For this reason, the multiple signal classification algorithm is applied to extract the dominant natural frequency in [12]. Reference [13] combined the natural frequency method and the traveling wave method, it uses the former to roughly detect the fault area, then uses the latter to accurately find out the arrival time of the traveling wave head. This method not only avoids the dead zone of the natural frequency method, but also improves the fault location accuracy. The fault analysis method constructs the equivalent equations according to the relationship between system parameters and the measured electric quantity, then locates the fault point by solving the equations. References [16] and [17] calculate the voltage distributions along the transmission lines from the both side measurements, then locate the fault point according to the principle that the voltage distribution difference at the fault point is the smallest. The key factor affecting the accuracy of the fault analysis method is the accuracy of the line model. The adopted transmission line model in [16] is the Bergeron model and that in [17] is the distributed parameter model which takes the multi-order distance infinitesimal into account. The former line model is less accurate, the latter is more accurate but the multi-order infinitesimal increases the calculation amount. Reference [18] analyzes the fault characteristics of pole-to-pole and pole-to-ground fault on VSC-HVDC transmission lines, and calculates the fault distance by the voltage reference comparison method. But it's affected by the transition resistance and the accuracy needs to be further improved.

Aiming at the two-terminal VSC-HVDC transmission system, this paper proposes a single ended fault location principle based on the transient characteristics analysis of the pole-to-pole and pole-to-ground fault. For the pole-to-pole fault, this paper divides the fault transient process into three stages, and utilizes the time-domain expression of DC current at the diode freewheel

stage to realize the fault location, and gives the identification criterion for judging whether the fault evolves to the diode freewheel stage. For the pole-to-ground fault, this paper takes the current from the opposite system into account, and derives the differential equation of the fault current. The fault distance and transition resistance are solved as the expression of the characteristic roots of the differential equation. Then the extended Prony algorithm is used to fit the data to extract the characteristic roots. The simulation results under PSCAD/EMTDC show that the accuracy of the proposed fault location principle meets the engineering requirement.

2. Analysis of transient characteristics of VSC-HVDC transmission fault

Since the conventional HVDC systems mostly adopt two-terminal structure, the two-terminal VSC-HVDC transmission system is analyzed in this paper. As is shown in Fig. 1, the VSC-HVDC system consists of converter stations at both sides and bipolar transmission lines, the connecting transformers are connected in Ynd, that is, the neutral point of the transformer grid side winding is directly earthed. This connection can cut off the zero-sequence current propagation path between the alternating current (AC) side and DC side. The neutral point of the DC side capacitor is also earthed to form symmetrical positive and negative DC transmission lines to reduce the insulation level of the DC line to ground.
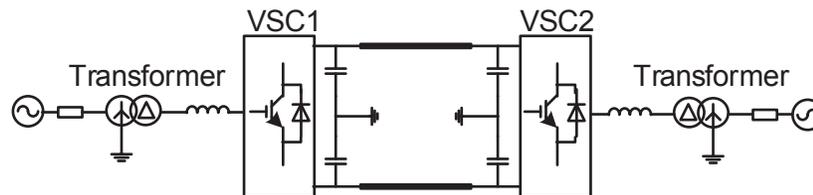

Fig. 1. Typical earthing mode of two-terminal VSC-HVDC

2.1. Analysis of pole-to-pole fault transient characteristics

The pole-to-pole fault is the most serious fault of VSC-HVDC transmission lines. The short circuit current will rise to several times the rated current within a few milliseconds, and will cause a huge impact on insulated gate bipolar transistors (IGBT).

The Fig. 2. shows the equivalent circuit of the pole-to-pole fault. The two-level VSC consists of six IGBTs and the freewheeling diodes $D_1 \sim D_6$ connected in antiparallel, and C is the DC side parallel capacitor. The IGBT can be instantaneously blocked after fault occurs due to its self-protection function. However, the anti-parallel diode is still connected to form a circuit between the AC system, DC side and the fault point, thus the DC side fault cannot be completely isolated. The fault transient process is analyzed below.

1. Capacitor discharge stage

After a pole-to-pole fault occurs on the transmission lines, during the initial stage, the DC side voltage u_{dc} is greater than the AC side line voltage, the parallel capacitor begins to discharge through the DC lines and the smoothing reactor. So, the influence of distributed capacitance
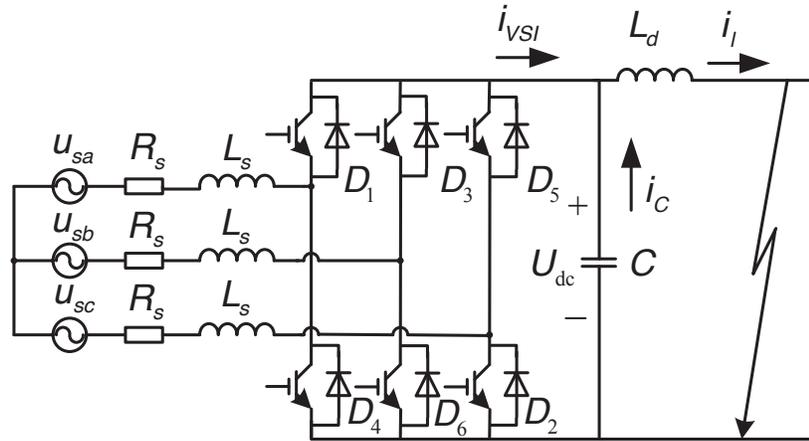
Fig. 2. Equivalent circuit of pole-to-pole fault

on the discharge process of transmission lines can be ignored. Therefore, the DC side forms a second-order discharge circuit, which can be listed as follows:

$$(L + L_d)C\frac{\mathrm{d}^2 u_{dc}}{\mathrm{d}t^2} + RC\frac{\mathrm{d}u_{dc}}{\mathrm{d}t} + u_{dc} = 0, \tag{1}$$

where: R and L are the equivalent resistance and inductance from the fault point to the DC bus, respectively, and L_d is the smoothing reactor at the DC bus. We assume that U_0, I_0 are the initial values of DC side voltage and current. Because the pole-to-pole fault is mostly metallic, its damping value meets $R < 2\sqrt{(L + L_d)/C}$, which is underdamped. Solved by the three-factor method of the second-order circuit, the DC voltage u_{dc} and the capacitor current i_c during this stage are [19]:

$$\begin{cases} u_{dc} = Ae^{-\sigma t}\sin(\omega t + \theta) \\ i_l = i_c = -C\dfrac{\mathrm{d}u_{dc}}{dt} = -A\sqrt{\dfrac{C}{(L + L_d)}}e^{-\sigma t}\sin(\omega t + \theta - \phi) \end{cases}, \tag{2}$$

where:

$$A = \sqrt{U_0^2 + \frac{(CU_0\sigma - I_0)^2}{(\omega C)}}$$

is the DC voltage amplitude,

$$\phi = \arctan\left(\frac{\omega}{\sigma}\right),$$

$$\omega = \sqrt{\frac{1}{[(L + L_d)C]} - \left[\frac{R}{(2L + 2L_d)}\right]^2}$$

is the frequency of DC voltage and current,

$$\sigma = \frac{R}{[2\,(L + L_d)]}$$

is the attenuation coefficient,

$$\theta = \arctan\left[\frac{U_o \omega C}{(C U_o \sigma - I_o)}\right].$$

From Equation (2), it can be seen that the capacitor discharge stage is a second-order un-derdamped oscillation process, and the DC side current will gradually oscillate and decay. The changing trend of the DC side voltage and current are mainly determined by the resistance and inductance values in the fault loop. The larger the resistance value and the smaller the inductance value, the higher the oscillation frequency and the faster the attenuation rate.

2. Diode natural commutation stage

As the capacitors continue to discharge, the DC voltage gradually decreases. When it is lower than the AC side line voltage, the AC system starts to feed current through freewheel diodes to the fault point. According to the natural commutation principle, the diodes are turned on and off alternately. Therefore, the DC side current i_l at this stage includes the AC side feed current i_{sac} and the capacitor discharge current i_c, as shown in Fig. 3.
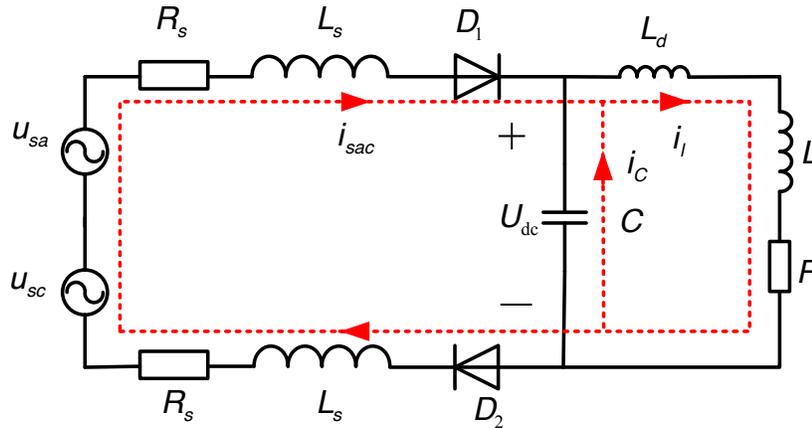

Fig. 3. Equivalent circuit diagram of D_1, D_2 conduction

Taking the conduction of phase-A and phase-C as an example, the response process of the circuit can be divided into two parts: zero-state response and zero-input response with the influence of the AC side feed. Suppose that the AC side line voltage at initial is:

$$U_{sac} = U_m \sin(\omega_s t + \alpha), \tag{3}$$

where: U_m is the amplitude of the AC side line voltage, ω_s is the AC system power frequency angular velocity, α is the initial phase angle. The zero-state response [20] is only generated by

the external excitation source u_{sac}, and the DC side current component i_{lzs} of the zero-state response is:

$$i_{lzs} = A \sin(\omega_s t + \alpha - \varphi), \tag{4}$$

where:

$$A = \frac{U_m}{\sqrt{M^2 + N^2}}$$

is the magnitude of the fault component,

$$\varphi = \arctan M/N$$

is the angle at which the fault component lags u_{sac},

$$M = \omega_s L_s \left[1 - \omega_s^2 C(L + L_d)\right] + \omega_s CRR_s + \omega_s(L + L_d),$$

$$N = R + \omega_s L_s CR - R_s \left[1 - \omega_s^2 CL + L_d)\right].$$

The zero-input response is produced by the original energy storage of the inductance and capacitance. According to the characteristics of the circuit, the differential equation is

$$\frac{\mathrm{d}i_{lzi}^3}{\mathrm{d}t^3} + A_1 \frac{\mathrm{d}i_{lzi}^2}{\mathrm{d}t^2} + A_2 \frac{\mathrm{d}i_{lzi}}{\mathrm{d}t} + A_3 = 0, \tag{5}$$

where: i_{lzi} is the DC current component in the zero-input response, the coefficients are expressed as:

$$A_1 = \frac{[R_s(L_d + L) + L_s + R]}{(L_s L)}, \qquad A_2 = \frac{(2R_s CR + 2L_s + L_d + L)}{(2L_s LC)}, \qquad A_3 = \frac{(R + R_s)}{2L_s LC}.$$

Substituting the above coefficient expression into Formula (5), according to Shengjin's formula, the characteristic roots of the differential equation are judged to consist of negative real roots and a pair of conjugate complex roots.

Therefore, the DC side current at this stage is superimposed of three kinds of components: the synchronous frequency sine component, the attenuated non-periodic component and the attenuated free oscillation periodic component.

3. Diode freewheel stage

As the capacitor discharge current rises rapidly, the capacitor voltage begins to drop, while the AC side feed current is far less than the capacitor discharge current, and the DC side current is still dominated by the capacitor discharge current. The capacitor discharge current will decay after it reaches the peak, the DC side current also begins to decay, and the inductor L changes from charging to discharging. Since the induced voltage at both ends of the inductor L is opposite to that of the capacitor C, u_{dc} will further discharge to zero. At this point, most of the energy stored in the capacitor is transferred to the inductor, and the back electromotive force of the inductor will make the six freewheeling diodes conduct at the same time. The DC side and the AC side are independent. The equivalent circuit is shown in Fig. 4.

Assuming that the DC line current at the u_{dc} zero-crossing moment is I_0, the DC short-circuit transient current during the diode freewheel stage is:

$$i_l = I_0 e^{-\frac{R}{L+L_d}t}. \tag{6}$$

It can be seen that the current on the DC side is an attenuated aperiodic component.
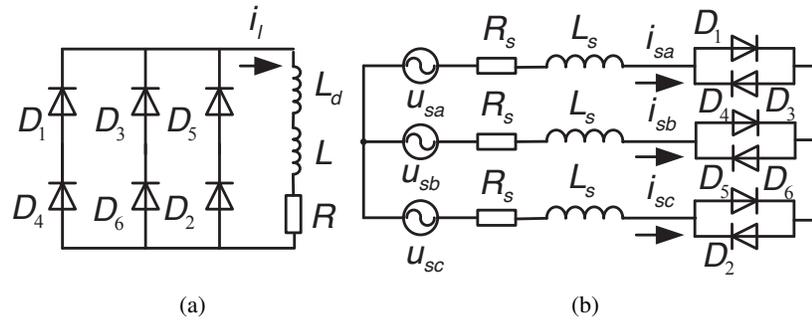
Fig. 4. Equivalent circuit of diode freewheel stage: DC side (a); AC side (b)

2.2. Analysis of pole-to-ground fault transient characteristics

Compared with the pole-to-pole fault, the pole-to-ground fault occurs more frequently. After the pole-to-ground fault occurs, both the rectifier and the inverter side will feed current to the fault point, so it is necessary to consider the contribution of the opposite system. The fault loop of the positive pole-to-ground fault in the capacitor discharge stage is shown in Fig. 5. Rec represents the rectifier side converter station, Inv represents the inverter side converter station, u_{rp}, u_{ip} represent the positive voltage of the rectifier side and the inverter side, i_{rp}, i_{rn} represent the positive and negative current on the rectifier side, i_{ip}, i_{in} represent the positive and negative currents on the inverter side, and i_f represents the current fed by the transmission lines to the fault point.
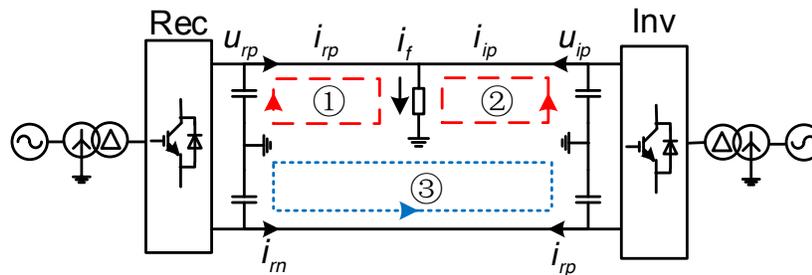

Fig. 5. Circuit loop of positive grounding fault

In this stage, the DC voltage u_{dc} is greater than voltage on the fault point, the capacitor is discharged through the DC line to the fault point, the discharge current flow path on the positive capacitor on the rectifier side is ①, that on the inverter side is ②, and the negative capacitors discharge loop is ③. On this basis, the converter station can be equivalent to the DC side parallel capacitor for analysis, as shown in Fig. 6.

The Kirchhoff voltage laws(KVL) equations of the rectifier side and the inverter side system are constructed as:

$$u_{rp} - R_1 \cdot i_{rp} - (L_1 + L_d)\frac{\mathrm{d}i_{rp}}{\mathrm{d}t} - R_f \cdot i_f = 0, \tag{7}$$
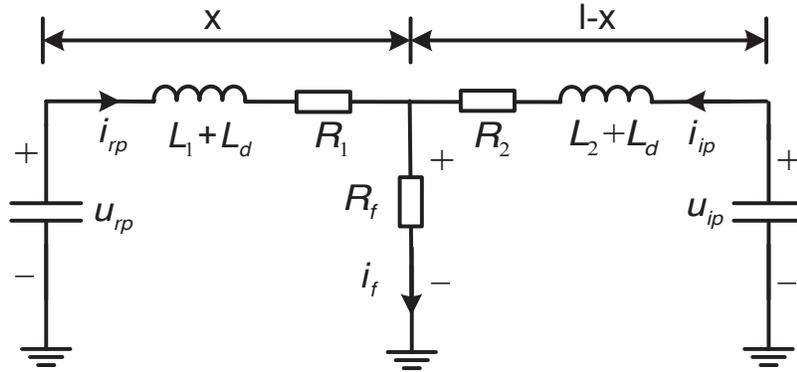
Fig. 6. Equivalent circuit of positive pole-to-ground fault

$$u_{ip} - R_2 \cdot i_{ip} - (L_2 + L_d) \frac{\mathrm{d}i_{ip}}{\mathrm{d}t} - R_f \cdot i_f = 0. \tag{8}$$

The positive current on the inverter side i_{ip} can be expressed as the following equation with the positive current on the rectifier side i_{rp}.

$$i_{ip} = \frac{1}{R_f} \left[u_{rp} - i_{rp} \left(R_1 + R_f \right) - \frac{\mathrm{d}i_{rp}}{\mathrm{d}t}(L_1 + L_d) \right]. \tag{9}$$

Differentiate the above formula

$$\frac{\mathrm{d}i_{ip}}{\mathrm{d}t} = \frac{1}{R_f} \left[\frac{\mathrm{d}u_{rp}}{\mathrm{d}t} - \frac{\mathrm{d}i_{rp}}{\mathrm{d}t} \left(R_1 + R_f \right) - \frac{\mathrm{d}^2 i_{rp}}{\mathrm{d}t^2}(L_1 + L_d) \right]. \tag{10}$$

After substitution and simplification, the expression containing only the positive current on the rectifier side is obtained by:

$$\frac{\mathrm{d}i_{rp}^4}{\mathrm{d}t^4} + A_1 \frac{\mathrm{d}i_{rp}^3}{\mathrm{d}t^3} + A_2 \frac{\mathrm{d}i_{rp}^2}{\mathrm{d}t^2} + A_3 \frac{\mathrm{d}i_{rp}}{\mathrm{d}t} + A_4 i_{rp} = 0. \tag{11}$$

The solution of the fourth-order differential equation is determined by the coefficients A_1, A_2, A_3, A_4. The value of each coefficient is only related to the fault distance x and transition resistance R_f, which are:

$$\begin{cases} A_1 = \dfrac{2r_0 l_0 x(l-x) + R L_d + R_f(L + 2L_d)}{l_0^2(l-x)x + L L_d + L_d^2}, & A_2 = \dfrac{L + 2L_d + \left(r_0^2 x(l-x) + R R_f\right) C}{C\left(l_0^2(l-x)x + L L_d + L_d^2\right)} \\ A_3 = \dfrac{R + 2R_f}{C\left(l_0^2(l-x)x + L L_d + L_d^2\right)}, & A_4 = \dfrac{1}{C^2\left(l_0^2(l-x)x + L L_d + L_d^2\right)} \end{cases}. \tag{12}$$

In Equation (12), r_0 represents the resistance per unit length of the DC line, l_0 represents the inductance per unit length of the DC line, $R = r_0 l$ represents the total resistance of the DC line,

$L = l_0 l$ represents the inductance of the DC line, L_d is the smoothing reactance at the DC outlet of the converter station, and l is the total length of the DC line.

The Appendix verifies that the characteristic root discriminant of Equation (11) is above zero, so the solution of the differential equation consists of a pair of conjugate complex roots and two different real roots [21]. The i_{rp} can be expressed as:

$$i_{rp}(t) = C_1 e^{\lambda_i t} + C_2 e^{\lambda_2 t} + C_3 e^{\alpha t} \sin \beta t + C_4 e^{\alpha t} \cos \beta t, \tag{13}$$

where: $C_1 e^{\lambda_i t}$, $C_2 e^{\lambda_2 t}$ are the attenuate aperiodic components, λ_1, λ_2 represent the attenuation coefficients; $C_3 e^{\alpha t} \sin \beta t$, $C_4 e^{\alpha t} \cos \beta t$ represent the damped free oscillation period component, α is the attenuation constant, β is the free oscillation angular frequency, corresponding to a pair of conjugate complex roots of the characteristic equation $\lambda_{3,4} = \alpha_k \pm i \beta_k$.

3. Method of fault location

3.1. Pole-to-pole fault location principle

3.1.1. Identification of different fault stages

When a pole-to-pole fault occurs, according to the analysis in chapter 2.1, there are four different fault stages. The fault characteristics of each stage are shown in Table 1, and the different stages can be distinguished according to it.

Table 1. Characteristics of different fault stages

	$\dfrac{\mathrm{d}u_{dc}}{\mathrm{d}t}$	$\dfrac{\mathrm{d}i_l}{\mathrm{d}t}$
Capacitor discharge stage	< 0	$\neq 0$
Diode natural commutation stage	$\neq 0$	$\neq 0$
Diode freewheel stage	0	< 0
Steady stage	0	0

The pole-to-pole fault location principle proposed in this paper is based on the diode freewheel stage. In order to identify the fault transient process that evolves to the diode freewheel stage, the identification criteria are given as follows:

$$\begin{aligned} &(3 \text{ consecutive points meet } |u_{dc}(t + \Delta t) - u_{dc}(t)| < U_{set}) \text{ and} \\ &(3 \text{ consecutive points meet } [i_l(t + \Delta t) - i_l(t)] < 0). \end{aligned} \tag{14}$$

In the equation, Δt is the sampling interval and U_{set} is the identification criterion threshold. In this paper, the threshold $U_{set} = 0.001 U_e$, U_e is the rated voltage. When the voltage and current meet the criterion, the fault stage is identified as entering the diode freewheel stage. In this stage, the DC side fault process is not affected by the AC side, and it is easy to identify it according to the DC voltage and current characteristics, so it can be used for fault location.

3.1.2. Fault location method

During the diode freewheel stage, the DC current contains only attenuated aperiodic components provided by the inductance in the DC side fault loop. Considering the existence of the smoothing reactor L_d, Equation (6) can be rewritten as:

$$i_l = I_0 e^{-\frac{r_0 x}{l_0 x + L_d} t},$$

(15)

where t is the time difference from the sampling moment to the initial moment at this stage.

Take the logarithm of (15), and the expression of the fault distance x is

$$x = \frac{-L_d \cdot \ln\left(\frac{i_l}{I_0}\right)}{r_0 \cdot t + l_0 \cdot \ln\left(\frac{i_l}{I_0}\right)}.$$

(16)

In order to improve the accuracy, n sampling points that meet the conditions are selected in the fault section and substituted into Equation (16) to calculate. Take the average of the results, and finally get the following equation for locating.

$$\overline{x} = \frac{1}{n} \sum_{i=1}^{n} \frac{-L_d \cdot \ln\left(\frac{i_{li}}{I_0}\right)}{r_0 \cdot t_i + l_0 \cdot \ln\left(\frac{i_{li}}{I_0}\right)}.$$

(17)

3.2. Pole-to-ground fault location

From the previous analysis, it can be known that the existence of the parallel capacitors and the line inductance will make the DC current contain attenuated oscillation periodic and attenuated aperiodic components. The fault distance x and the transition resistance R_f will affect the transient process of the DC current. Therefore, it's difficult to obtain the analytical formula of the fault current by Equation (11), we proposed a method of identifying the parameters of characteristic roots to locate the fault point.

It's necessary to analyze the characteristics of the solution of (11). The characteristic equation corresponding to Equation (11) is:

$$\lambda^4 + A_1 \lambda^3 + A_2 \lambda^2 + A_3 \lambda + A_4 = 0.$$

(18)

This fourth-order equation must correspond to four characteristic roots, assume them as λ_1, λ_2, λ_3, λ_4, and rewrite the above formula into the form of factor multiplication as [22]:

$$(\lambda - \lambda_1)(\lambda - \lambda_2)(\lambda - \lambda_3)(\lambda - \lambda_4) = 0.$$

(19)

Expanding and simplifying Equation (19) and comparing it with Equation (18), the relationship between the coefficients and the characteristic roots is obtained as follows:

$$\begin{cases} A_1 = -\lambda_1 + \lambda_2 + \lambda_3 + \lambda_3), & A_2 = \lambda_1\lambda_2 + \lambda_1\lambda_3 + \lambda_1\lambda_4 + \lambda_2\lambda_3 + \lambda_2\lambda_4 + \lambda_3\lambda_4 \\ A_3 = -(\lambda_1\lambda_2\lambda_3 + \lambda_1\lambda_2\lambda_4 + \lambda_1\lambda_3\lambda_4 + \lambda_2\lambda_3\lambda_4), & A_4 = \lambda_1\lambda_2\lambda_3\lambda_4 \end{cases}.$$

(20)

Substitute Equation (12) into Equation (20), the transition resistance R_f and fault distance x are obtained as:

$$R_f = -\frac{1}{2C}\left(\frac{1}{\lambda_1} + \frac{1}{\lambda_2} + \frac{1}{\lambda_3} + \frac{1}{\lambda_4}\right) - \frac{r_0 l}{2}, \tag{21}$$

$$x_{1,2} = \frac{l}{2} \pm \frac{1}{2l_0}\left(4L_d^2 + l_0^2 l^2 + 4l_0 l L_d - \frac{4}{\lambda_1 \lambda_2 \lambda_3 \lambda_4 C^2}\right)^{\frac{1}{2}}. \tag{22}$$

The fault distances solved by Equation (22) have two roots x_1, x_2 ($x_1 < x_2$), which are symmetric about the midpoint of the line. In order to eliminate the false root, the difference between the calculated voltage and the actual measured voltage is used. Name the initial end of the line as M (rectifier side) and the terminal as N (inverter side). We assumed that the voltage at the distance x from the initial end be $u(x, t)$, and the current at the initial end be i_M. According to the equation of the uniform transmission line, the voltage at the beginning u_M can be obtained by:

$$u_M = \frac{u(x, t) + i_M Z_c \sinh \gamma x}{\cosh \gamma x}, \tag{23}$$

where:

$$Z_c = \sqrt{\frac{(r_0 + j\omega l_0)}{(G_0 + j\omega C_0)}},$$

$$\gamma = \sqrt{(r_0 + j\omega l_0)(G_0 + j\omega C_0)},$$

r_0, l_0, G_0 and C_0 are, respectively, the resistance, inductance, conductance and capacitance per unit line length, ω is the frequency corresponding to the characteristic roots λ_3, λ_4.

Substitute x_2 into Equation (7) to obtain the calculated voltage at the fault point.

$$u_{fx2} = i_f R_f = u_{rp} - R_0 \cdot x_2 \cdot i_{rp} - (L_0 \cdot x_2 + L_d)\frac{di_{rp}}{dt}. \tag{24}$$

Then, substitute u_{fx2} into Equation (23) to replace $u(x, t)$ to obtain the calculated voltage at the exit of the rectifier side.

$$u_{Mx2} = \frac{u_{fx2} + i_M Z_c \sinh \gamma x_2}{\cosh \gamma x_2}. \tag{25}$$

When the real fault distance is x_2, the calculated fault u_{Mx2} and the actual measured value u_M are equal. When the real fault distance is x_1, the calculated voltage u_{Mx2} and the actual measured value u_M are not equal. Therefore, by comparing the calculated voltage value with the actual measured voltage value, a simple and reliable criterion for identifying the false root of fault distance is proposed as follows:

$$|u_{Mx2} - u_M| > K_{rel} \cdot 5\% U_N. \tag{26}$$

Determine the actual fault points as x_1 when consecutive points meet (26).

There, U_N is the rated value of DC voltage, $K_{rel} = 1.15$ is the reliability coefficient. When the calculated value u_{Mx2} of port voltage and the actual value u_M meet the above criteria, determine the actual fault point as x_1; otherwise, determine the actual fault point as x_2.

The key of fault location is to accurately obtain λ_1, λ_2, λ_3, λ_4 from the sampling data. The estimation model of the extended Prony algorithm has good adaptability to the fault current represented in Equation (13), and the use of the extended Prony algorithm can effectively avoid the iterative problem caused by the nonlinear solution. So, this paper uses the extended Prony algorithm to fit the sampling data and calculate the characteristic roots.

Assume that there are N measured data $x(n)$, $n = 0 \sim N - 1$, the extended Prony algorithm estimation model $\hat{x}(n)$ in discrete time form is:

$$\hat{x}(n) = \sum_{i=1}^{p} A_i e^{\alpha_i n \Delta t} \cos\left(2\pi f_i n \Delta t + \theta_i\right) = \sum_{i=1}^{p} b_i z_i^n, \tag{27}$$

where:

$$b_i = A_i \exp\left[j\theta_i\right],$$
$$z_i = \exp\left[(\alpha_i + j2\pi f_i)\Delta t\right],$$

p is the order of the model; A_i, f_i, θ_i, α_i are the amplitude, frequency, initial phase angle and attenuation factor; Δt is the sampling interval. References [23,24] presented the numerical method for solving the four characteristic parameters. Combined with Equation (27), the characteristic roots $\lambda_i (i = 1, 2, 3, 4)$ in Equation (13) are:

$$\lambda_i = \alpha_i + i2\pi f_i = \ln|z_i|/\Delta t + \arctan\left[\text{Im}(z_i)/\text{Re}(z_i)\right]/2\pi\Delta t. \tag{28}$$

4. Simulation and verification

4.1. Parameters and oscillograms of simulation

A two-terminal VSC-HVDC transmission system has been modelled in PSCAD/EMTDC. The rectifier side adopts constant active power and constant reactive power control, the inverter side adopts constant DC voltage and constant AC voltage control. The parameters of HVDC transmission systems are listed in Table 2. A data sampling frequency of 5 kHz is adopted, and the data is imported into MATLAB for verification.

The pole-to-pole fault is set at the midpoint of the DC line (100 km), and the fault time is set as 2.0 s. The simulation oscillogram is shown in Fig. 7 below.

Fig. 7 shows that the transient process of the pole-to-pole fault consists of four stages: the capacitor discharge stage, diode natural commutation stage, the diode freewheel stage and steady stage. During the capacitor discharge stage, the DC voltage drops while the fault current increases rapidly, the current flowing through the freewheeling diodes is zero, and fault current is only provided by the parallel capacitor discharge current on the DC side. When the DC voltage drops to the AC side voltage, the AC side system starts to feed current into the fault point, and the fault transient process enters the diode free commutation stage. Once the DC voltage drops to zero, the back electromotive force of the inductor will make the six freewheeling diodes conduct at the same time, the DC side and the AC side are independent, so the fault transient process will enter the diode freewheeling stage, the fault current is only provided by the inductance on the DC side,

① Capacitor discharge stage; ② Diode natural commutation stage;
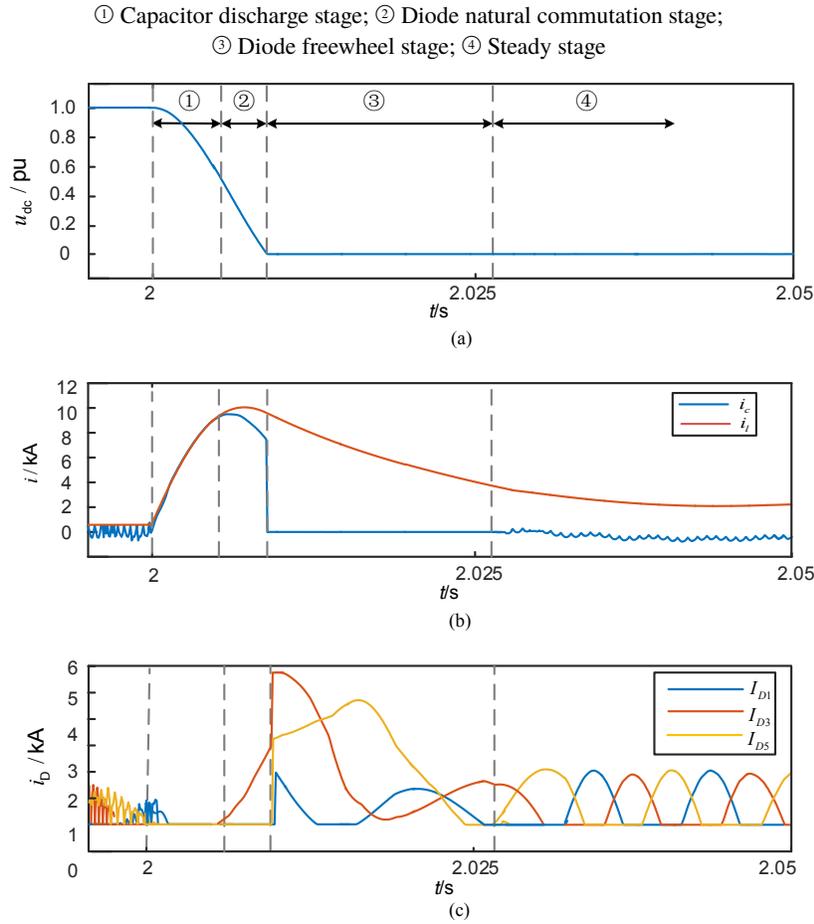③ Diode freewheel stage; ④ Steady stage

Fig. 7. Oscillogram of pole-to-pole fault transient stages: DC voltage on rectifier side (a); currents in fault
line and capacitor on rectifier side (b); currents in common-anode diodes (c)

and the overcurrent flowing through the freewheeling diodes reaches the peak at the start of this
stage. Thereafter, the fault enters the steady-state stage, the DC side is equivalent to the parallel
connection of capacitance and fault loop impedance, and the current is only composed of the
current fed from the AC side system.

A positive pole-to-ground with 10 Ω transition resistance is set at the line midpoint, and the
fault time is set as 2.0 s. Sample data from the rectifier side locates the fault point. In Fig. 2, u_{dc} is
the DC voltage between positive and negative poles, u_{rp} is the voltage of positive pole-to-ground,
u_{rn} is the voltage of negative pole-to-ground, i_l is the current of the DC line on the rectifier side.

As shown in Fig. 8, u_{rp} shows a trend of oscillation and attenuation, eventually tends to zero.
Under the control of the system, u_{rn} drops to a negative rated DC voltage, and u_{dc} tends to the
rated value after the oscillation. The fault current in the DC line i_l is composed of attenuated
periodic components and attenuated non-periodic components.

Table 2. Parameters of VSC-HVDC system

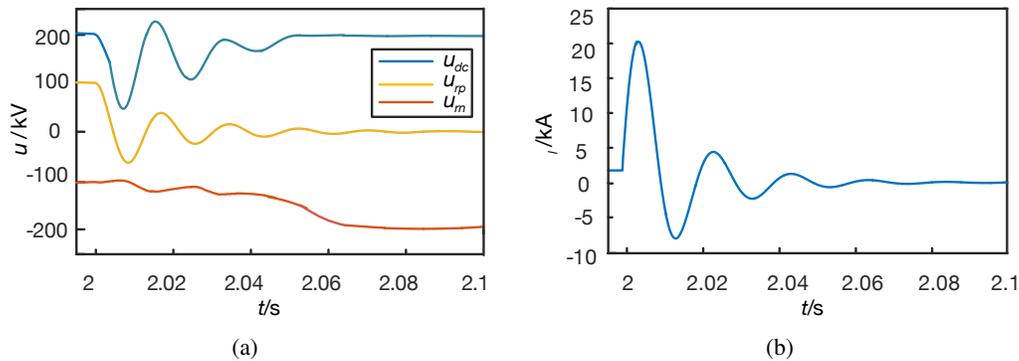| Components	Parameters	Value
DC lines	Rated DC voltage	±200 kV
	Inductance in per unit length	0.000159 H/km
	Resistance in per unit length	0.0139 Ω/km
	Total length	200 km
	Smoothing reactor	10 mH
	Parallel capacitors	1 000 μF
VSC converter stations at both ends	Rated AC voltage	110 kV
	Transformer rated capacity	400 MVA
	Transformer rated ratio	200 kV/110 kV
	Frequency	50 Hz

Fig. 8. pole-to-ground fault voltages and current on rectifier side: voltages (a); DC fault current (b)

4.2. Verification of fault location

In order to verify the effectiveness of the pole-to-ground fault location method, set the line midpoint (100 km) to have the positive pole-to-ground fault with 10 Ω transition resistance, sample the positive current data of the rectifier side, and use the extended Prony algorithm to fit the fault current. The fitting result contains the characteristic parameters of each component in current: amplitude, frequency, an initial phase angle, decay factor. Substitute the characteristic parameters into Equation (13), and obtain the fitting analytical formula of the fault current.

$$\{i_{rp}\}_{kA} = 2.769e^{-871.150t} + 1.480e^{-44.325t} + 2.921e^{-17.967t}\sin 62.284\pi t - \\ -3.697e^{-17.967t}\cos 62.284\pi t \qquad (29)$$

The four characteristic roots of the characteristic equation can be obtained by substituting α_i and f_i into Equation (28).

$$\lambda_1 = -871.150; \qquad \lambda_2 = -44.325; \qquad \lambda_{3,4} = -17.967 \pm i62.284\pi . \tag{30}$$

Substitute $l_0 = 0.000159$ mH, $L_d = 10$ mH, $l = 200$ km, $C = 1000$ μF and the above characteristic roots into Equation (22), the fault distance is solved as follows:

$$\begin{aligned}
x_{1,2} &= \frac{l}{2} \pm \frac{1}{2l_0}\left(4L_d^2 + l_0^2 l^2 + 4l_0 l L_d - \frac{4}{\lambda_1 \lambda_2 \lambda_3 \lambda_4 C^2}\right)^{\frac{1}{2}} = \\
&= 100 \pm 3144.65 \cdot \left(0.00268 - \frac{4000000}{871.150 \cdot 44.325 \cdot (17.967^2 + 62.284^2\pi^2)}\right)^{\frac{1}{2}} .
\end{aligned} \tag{31}$$

The two solutions of the fault distance are:

$$x_1 = 98.427, \qquad x_2 = 101.572. \tag{32}$$

According to the criterion in Equation (26), x_1 is the real root of the fault distance.

Table 3 lists the results of characteristic roots fitted by the extended Prony algorithm of the pole-to-ground fault.

Table 3. The characteristic results of roots extracted by extended Prony algorithm of pole-to-ground fault

Fault distance/km	Transition resistance/Ω	λ_1	λ_2	$\lambda_{3,4}$
10	1	−901.290	−48.921	−106.850 ± 193.391i
	10	−1171.235	−44.289	−134.865 ± 202.884i
	100	−1114.264	−49.329	−22.570 ± 195.701i
100	1	−604.871	−63.843	−186.406 ± 62.121i
	10	−871.150	−44.325	−17.967 ± 195.671i
	100	−779.621	−49.552	−21.537 ± 195.263i
190	1	−901.287	−48.938	−106.847 ± 193.358i
	10	−1169.861	−44.057	−13.486 ± 202.873i
	100	−1112.071	−49.377	−22.461 ± 195.722i

The error of location is calculated by the following equation:

$$\text{error} = \frac{|\text{calculated fault distance} - \text{real fault distance}|}{\text{total length}} \times 100\% . \tag{33}$$

Change the fault types, fault distance and the value of the transition resistance, the fault location results are shown in Table 4.

The results of the fault location show that the method proposed in this paper can avoid the influence of transition resistance effectively in the case of the pole-to-ground fault, and accurate fault location can be realized at both the near and far end of the DC bus.

Table 4. Fault location results

Fault type	Fault distance/km	Transition resistance/Ω	Locating distance/km	error %
Pole-to-pole	10	Metallic short circuit	10.161	0.081
	100		100.181	0.090
	190		190.165	0.083
Pole-to-ground	10	1	9.683	0.159
		10	10.055	0.028
		100	10.609	0.305
	100	1	101.415	0.708
		10	98.427	0.787
		100	101.476	0.738
	190	1	190.324	0.162
		10	189.270	0.365
		100	189.178	0.411

5. Conclusion

This paper proposed a simple and reliable method for the pole-to-pole fault according to which the time-domain expression of the DC current during the diode freewheel stage was used to locate the fault point, and the identification criterion for judging whether the fault evolves to the diode freewheel stage was presented. Considering the enhancing effect of the opposite system on the fault current, the DC side pole-to-ground fault network was equated to a fourth-order circuit model, the relationship of transition resistance and fault distance with the characteristic roots of the fault current differential equation were derived, and the extended Prony algorithm was utilized for data-fitting to extract characteristic roots to realize fault location. In principle, the influence of transition resistance is eliminated, and the accuracy meets engineering requirements.

The proposed fault location method used single-terminal transient data after the fault occurs, there is no requirement of clock synchronization for both terminals of the system, and a sampling frequency of 5 kHz can meet the accuracy requirement.

Appendix

In order to analyse the transient characteristics of the pole-to-ground fault, it's necessary to clarify the character of characteristic roots. To simplify the expression, introduce intermediate variables D, E, F.

$$D = 3(A_1^2 - 8A_2)^2, \quad E = 3A_1^4 + 16A_2^2 - 16A_1A_2 + 16A_1A_3 - 64A_4$$
$$F = A_1^3 - 4A_1A_2 + 8A_3 \tag{A1}$$

Combining the permutation group solution with Shengjin's formula, the characteristic of the roots can be judged by the discriminant equation Δ. Therefore, Δ can be expressed as a multinomial expression with respect to the fault distance x and the transition resistance R_f.

$$\Delta = -3D^2E^2 - 54DEF + 12D^3F + 81F^2 + 12E^2 = f(A_1A_2A_3A_4) = z(xR_f). \quad \text{(A2)}$$

Substitute the system parameters into Equation (A2), and set the value of the fault distance x and transition resistance R_f in Matlab changed [0, 200 km] and [0, 100 Ω], the image of $z(xR_f)$ is shown as:
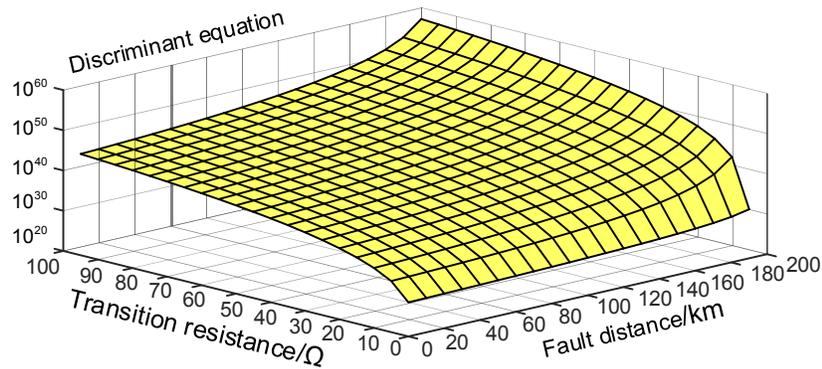

Fig. A1. The relationship between discriminant equation, fault distance and transition resistance

As shown in Fig. A1, $\Delta = z\left(x, \ R_f\right) > 0$, the solution of Equation (11) is composed of a pair of conjugate complex roots and two different real roots.

References

[1] Flourentzou N., Agelidis V.G., Demetriades G.D., *VSC-Based HVDC Power Transmission Systems: An Overview*, IEEE Transactions on Power Electronics, vol. 24, no. 3, pp. 592–602 (2009).

[2] Li C., Li Y., Guo J., *Research on emergency DC power support coordinated control for hybrid multi-infeed HVDC system*, Archives of Electrical Engineering, vol. 69, no. 1, pp. 5–21 (2020).

[3] Banu G., Suja S., *Fault location technique using GA-ANFIS for UHV line*, Archives of Electrical Engineering, vol. 63, no. 2, pp. 247–262 (2014).

[4] Yang L., Wang B., Dong X., *Overview of fault location methods in high voltage direct current transmission lines*, Automation of Electric Power Systems, vol. 42, no. 8, pp. 185–191 (2018).

[5] Jamali S., Mirhosseini S.S., *Protection of transmission lines in multi-terminal HVDC grids using travelling waves morphological gradient*, International Journal of Electrical Power and Energy Systems, vol. 108, pp. 125–134 (2019).

[6] Fan Ch., Jiang J., Guo Y., *Development and applications of traveling wave fault location on transmission lines*, Proceedings of the CSU-EPSA, vol. 29, no. 4, pp. 129–134 (2017).

[7] Li D., Ukil A., Satpathi K., *Improved S Transform Based Fault Detection Method in VSC Interfaced DC System*, IEEE Transactions on Industrial Electronics, vol. 68, iss. 6, pp. 5024–5035 (2020), DOI: 10.1109/TIE.2020.2988193.

[8]   Qin J., Peng L., Wang H., *Single terminal methods of traveling wave fault location in transmission line using wavelet transform*, Automation of Electric Power Systems, vol. 29, no. 19, pp. 62–65+86 (2005).

[9]   Xu X., Sheng G., Liu Y., *Fault location method for transmission lines based on distributed traveling wave detection*, Proceedings of the Chinese Society of Universities for Electric Power System and its Automation, vol. 24, no. 3, pp. 134–138 (2012).

[10] He Z., Liao K., Li X., Lin S., Yang J., Mai R., *Natural Frequency-Based Line Fault Location in HVDC Lines*, IEEE Transactions on Power Delivery, vol. 29, no. 2, pp. 851–859 (2014).

[11] He Z., Liao K., *Natural frequency-based protection scheme for voltage source converter-based high-voltage direct current transmission lines*, IET Generation, Transmission and Distribution, vol. 9, no. 13, pp. 1519–1525 (2015).

[12] Cai X., Song G., Gao S., *A novel fault-location method for VSC-HVDC transmission lines based on natural frequency of current*, Proceedings of the CSEE, vol. 31, no. 28, pp. 112–119 (2011).

[13] Zhang Y., Wang H., Li T., *Combined single-end fault location method for LCC-VSC hybrid HVDC transmission lines*, Automation of Electric Power Systems, vol. 43, no. 21, pp. 187–199 (2019).

[14] Suonan J., Gao S., Song G., Jiao Z., Kang X., *A Novel Fault-Location Method for HVDC Transmission Lines*, IEEE Transactions on Power Delivery, vol. 25, no. 2, pp. 1203–1209 (2010).

[15] Yanxia Z., Jian W., Huilan J., Fang Z., *A Novel Fault Location Method for Hybrid-HVDC Transmission Line*, 2019 IEEE Power and Energy Society General Meeting (PESGM), Atlanta, GA, USA, pp. 1–5 (2019).

[16] Song G., Zhou D., Jiao Z., *A novel fault location principle for HVDC transmission lines*, Automation of Electric Power Systems, vol. 31, no. 24, pp. 57–61 (2007).

[17] Kang L., Tang K., Luo J., *Two-terminal fault location of monopolar earth fault in HVDC transmission lines*, Power System Technology, vol. 38, no. 8, pp. 2268–2273 (2014).

[18] Jin Y., Fletcher J.E., O'Reilly J., *Short- circuit and ground fault analyses and location in VSC-based DC network cables*, IEEE Transactions on Industrial Electronics, vol. 59, no. 10, pp. 3827–3837 (2012).

[19] Liu D., Wei T., Huo Q., *DC side line-to-line fault analysis of VSC-HVDC and DC-fault-clearing methods*, 2015 5-th International Conference on Electric Utility Deregulation and Restructuring and Power Technologies (DRPT), Changsha, China, pp. 2395–2399 (2015).

[20] Dessouky S.S., Fawzi M., Ibrahim H.A., Ibrahim N.F., *DC Pole to Pole Short Circuit Fault Analysis in VSC-HVDC Transmission System*, 2018 Twentieth International Middle East Power Systems Conference (MEPCON), Cairo, Egypt, pp. 900–904 (2018).

[21] Ke J., Meng L.I., Shu B.T., *A voltage resonance-based single-ended online fault location algorithm for DC distribution networks*, Sciences China Technological Sciences, vol. 59, no. 5, pp. 721–729 (2016).

[22] Hwang K.S., Chang F.C., Chiou J.Y., *A numerical approach to fast evaluation of time-invariant system responses*, International Journal of Computer Mathematics, vol. 73, no. 3, pp. 361–369 (2000).

[23] Liu D., Hu W., Chen Z., *SVD-TLS extending Prony algorithm for extracting UWB radar target feature*, Journal of Systems Engineering and Electronics, vol. 19, no. 2, pp. 286–291 (2008).

[24] Xu M.M., Xiao L.Y., Wang H.F., *A prony-based method of locating short-circuit fault in DC distribution system*, 2-nd IET Renewable Power Generation Conference (RPG 2013), Beijing, China, pp. 1–4 (2013).